New Journal of Physics
The open access journal at the forefront of physics

Deutsche Physikalische Gesellschaft DPG IOP Institute of Physics

PAPER • OPEN ACCESS

# Spin decoherence processes in the S = 1/2 scalene triangular cluster ($Cu_3(OH)$)

To cite this article: A N Ponomaryov *et al* 2015 *New J. Phys.* **17** 033042

New Journal of Physics
The open access journal at the forefront of physics

Deutsche Physikalische Gesellschaft DPG
IOP Institute of Physics

Published in partnership with: Deutsche Physikalische Gesellschaft and the Institute of Physics

OPEN ACCESS

RECEIVED
15 January 2015

REVISED
15 February 2015

ACCEPTED FOR PUBLICATION
23 February 2015

PUBLISHED
27 March 2015



PAPER

# Spin decoherence processes in the $S = \frac{1}{2}$ scalene triangular cluster ($Cu_3(OH)$)

A N Ponomaryov[1,2], N Kim[3], Z H Jang[4], J van Tol[5,6], H-J Koo[7], J M Law[2], B J Suh[8], S Yoon[3] and K Y Choi[1]

[1] Department of Physics, Chung-Ang University, Seoul 156-756, Korea
[2] High Magnetic Field Laboratory, Helmholtz Zentrum Dresden-Rossendorf, Dresden D-01328, Germany
[3] Department of Bio & Nano Chemistry, Kookmin University, Seoul 136-702, Korea
[4] Department of Physics, Kookmin University, Seoul 136-702, Korea
[5] Department of Chemistry and Biochemistry, Florida State University, Tallahassee, Fl 32306, USA
[6] National High Magnetic Field Laboratory, Florida State University, Tallahassee, Fl 32310, USA
[7] Department of Chemistry and Research Institute for Basic Sciences, Kyung Hee University, Seoul 130-701, Korea
[8] Department of Physics, The Catholic University of Korea, Bucheon 420-743, Korea

**E-mail:** yoona@kookmin.ac.kr **and** kchoi@cau.ac.kr

**Keywords:** molecular magnets, spin decoherence, spin triangular cluster

Supplementary material for this article is available online

## Abstract

We report the synthesis and magnetic properties of the molecular cluster $Cu_3(\mu_3\text{–OH})(\mu\text{-OH})(\mu\text{-}O_2Ar^{4F-Ph})_2(py)_3(OTf)_2$, abbreviated as ($Cu_3(OH)$). Using magnetization, electron paramagnetic resonance and spin dimer analysis, we derive a microscopic magnetic model of ($Cu_3(OH)$) and measure the electron $T_1$ and $T_2$ relaxation times. The $Cu^{2+}$ ions are arranged to form a distorted triangular structure with the three different exchange coupling constants $J_1 = -43.5$ K, $J_2 = -53.0$ K, and $J_3 = -37.7$ K. At $T = 1.5$ K $T_1$ is of the order of $10^{-4}$ s and $T_2$ is evaluated to be 0.26 $\mu$s. We find that the temperature dependence of $1/T_1$ and $1/T_2$ is governed by Orbach process and spin bath fluctuations, respectively. We discuss the role of spin–phonon mechanism in determining a spin decoherence time in a class of spin triangular clusters.

## 1. Introduction

Over the last decade, there has been a huge resurgence of interest in molecular magnets with the aim of elucidating the crossover from quantum to classical physics [1]. Molecular magnets as nanoscale quantum objects lead to a variety of quantum effects and potential applications to spintronics and quantum computing [2–4]. The prominent examples include quantum tunneling of magnetization [5, 6], a quantized rotation of a Néel vector [7–10], Berry phase interference [11], Landau–Zener effect [12], and a coherent manipulation of spins [13–15].

The $S = 1/2$ spin triangle represents one of the most interesting class among molecular magnets [16–19]. The antiferromagnetically coupled spin triangle provides the basic building unit for frustrated magnetism. Its chirality can induce magnetoelectric coupling as well as observations of magnetization hysteresis when the field sweep rate is an order of electron spin–lattice relaxation time [18, 20–24]. From the material point of view, the spin triangular core structure is realized in diverse molecular metallo-organic compounds; ($V_{15}$)[15–19], ($V_6$) [20, 21], and ($Cu_3$) clusters [22–24], the chiral ($Dy_3$) cluster [25], the two corner-sharing triangles ($Cu_5$) [26] and the giant icosidodecahedral keplerates ($Mo_{72}Fe_{30}$) [27].

An alternating sequence of two different isosceles antiferromagnetic spin triangles provides a genuine scheme for quantum gates [28–30]. This possibility has been experimentally tested in the isosceles triangle clusters ($Cu_3$–$X$) ($X$ = As, Sb) impregnated in nanoporous silicon [31]. The entanglement and manipulation of electron spins is achieved by using a pulsed electron spin resonance [31]. The spin coherence time reaches an order of microseconds. However, the coherence time is found to be limited by structural distortions from an

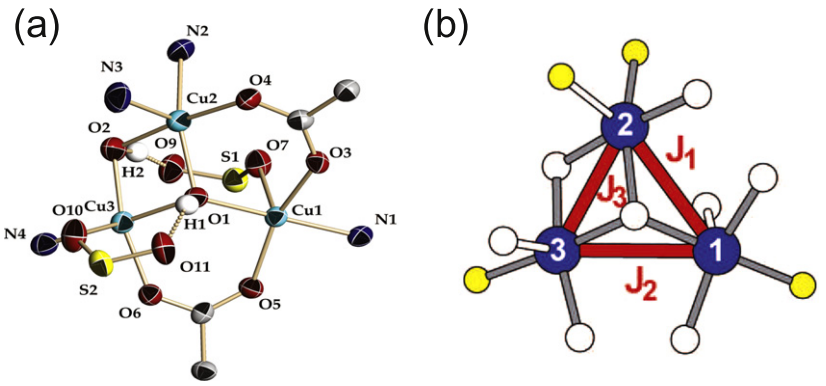


**Figure 1.** (a) ORTEP diagram of ($Cu_3(OH)$). For clarity, the aromatic rings of $Ar^{4F-Ph}CO_2^-$ ligands, pyridine, and triflate are omitted and hydrogen bonding interactions are depicted with dotted lines. (b) $Cu_3O_8N_4$ cluster unit in ($Cu_3(OH)$), where the blue, white, and yellow circles represent Cu, O, and N atoms, respectively. The gray cylinders indicate the Cu–O and Cu–N bonds in an equatorial plane. The red cylinders are the spin exchange paths, $J_1$, $J_2$, and $J_3$.

equilateral triangle and dynamic spin–phonon coupling. Thus, it is necessary to investigate a broad class of spin triangular clusters to rationalize key factors to govern relaxation processes.

We here report on the magnetic behavior and spin dynamics of $Cu_3(\mu_3\text{-OH})(\mu\text{-OH})(\mu\text{-}O_2Ar^{4F-Ph})_2(py)_3(OTf)_2$ (hereinafter abbreviated as ($Cu_3(OH)$)). It forms the distorted scalene triangle, yielding three nonequivalent Cu(II) positions, denoted by Cu1, Cu2, and Cu3 (see figure 1). Cu1 and Cu3 sites have slightly distorted $NO_4$ square pyramids while Cu2 site has a $N_2O_3$ square pyramidal surrounding. The pyramids are elongated axially due to Jahn–Teller distortion.

The three Cu(II) sites are linked by the oxygen atom of an hydroxo ($OH^-$) unit with Cu–O1 bond distances of 1.941(4), 2.023(4) and 1.990(5) Å. The Cu1 site is additionally bridged to each Cu2 and Cu3 site by two terphenyl-based carboxylates with a Cu ⋯ Cu separation of 3.2832(13) Å and 3.3920(13) Å, respectively. In contrast, Cu2 and Cu3 ions are linked by the additional $OH^-$ unit, instead of the carboxylate ligand, with a Cu ⋯ Cu separation of 2.9770(12) Å. The bridged hydroxide and terminal monodentate triflates create a tight intra-cluster network of hydrogen bonds with an average O ⋯ O separation of ca. 2.922 Å. Such hydrogen bonding interactions may help assemble the $Cu_3$ ($\mu_3$–OH) ($\mu_2$–OH) core. The closest intermetallic distance between the triangular clusters in the crystal lattice is 8.504 Å. The large separation suggests that there are no significant interactions between ($Cu_3(OH)$) triangular clusters and the major magnetic coupling interaction originates from exchange couplings between three copper(II) ions within the triangular cluster.

In this work, we report spin dimer analysis, magnetization, and electron spin resonance measurements of ($Cu_3(OH)$). Our major experimental finding is that the spin–lattice relaxation rate is dominated by Orbach process in the narrow low-temperature range of T = 1.45–2.4 K. This phonon mechanism provides an effective route to limit a spin decoherence time.

## 2. Experimental details

Crystals of ($Cu_3(OH)$) were prepared by the procedure described in supplementary materials. A crystal structure was characterized by a single crystal x-ray diffractometer. The results are summarized in tables 1 and 2 of supplementary materials (stacks.iop.org/NJP/17/033042/mmedia).

Magnetic susceptibility $\chi(T)$ was measured by quantum design MPMS SQUID in the temperature range of T = 2–220 K under an applied field of $\mu_0 H = 0.1$ T. The $M(H)$ curve was measured at $T = 2$ K in fields up to 14 T using the vibrating sample magnetometer (VSM) of quantum design PPMS. In addition, pulsed field magnetization measurements were carried out at the Dresden High Magnetic Field Laboratory with a pulsed field magnet (20 ms duration) and a standard induction method at $T = 1.5$ K [32].

Continuous and pulse electron paramagnetic resonance (EPR) experiments were performed by using 240 GHz superheterodyne detection scheme quasi-optical spectrometer, developed at the National High Magnetic Field Laboratory, Tallahassee, USA.

**Table 1.** List of exponents $\zeta_i$ ($i = 1, 2$) and valence shell ionization potentials $H_{ii}$ of Slater-type orbitals $\chi_i$ used for the extended Hückel tight-binding calculation.[a]

| Atom | $\chi_i$ | $H_{ii}$ (eV) | $\zeta_1$ | $C_1$ | $\zeta_2$ | $C_2$ |
|---|---|---|---|---|---|---|
| Cu | 4s | −11.4 | 2.151 | 1.0 | | |
| Cu | 4p | −6.06 | 1.370 | 1.0 | | |
| Cu | 3d | −14.0 | 7.025 | 0.4473 | 3.004 | 0.6978 |
| O | 2s | −32.3 | 2.688 | 0.7076 | 1.675 | 0.3745 |
| O | 2p | −14.8 | 3.694 | 0.3322 | 1.659 | 0.7448 |
| N | 2s | −26.0 | 2.261 | 0.7297 | 1.425 | 0.3455 |
| N | 2p | −13.4 | 3.249 | 0.2881 | 1.499 | 0.7783 |

[a] $H_{ii}$ are the diagonal matrix elements $\langle i\,|H_{\rm eff}|\,i\rangle$, where $H_{\rm eff}$ is the effective Hamiltonian. In our calculations of the off-diagonal matrix elements $H_{ij} = \langle i\,|H_{\rm eff}|\,j\rangle$, the weighted formula was used. See [38].

**Table 2.** Relative strengths of spin exchange interactions evaluated from spin dimer analysis and exchange coupling constants extracted from a fit to experimental data.

| Exchange path | $x = 0.00$ | $x = 0.025$ | $x = 0.05$ | Exp (K) |
|---|---|---|---|---|
| $J_1$ | 0.89 | 0.86 | 0.82 | −43.5 |
| $J_2$ | 1.00 | 1.00 | 1.00 | −53.0 |
| $J_3$ | 0.51 | 0.62 | 0.71 | −37.7 |

## 3. Results and discussion

### 3.1. Spin dimer analysis

In order to estimate the exchange coupling constants, we made spin dimer analysis. A spin exchange parameter $J$ can be written as $J = J_{\rm F} + J_{\rm AF}$, where $J_{\rm F}$ (>0) is the ferromagnetic component and $J_{\rm AF}$ (<0) is the antiferromagnetic component. For a spin dimer in which each spin site contains unpaired spin, $J_{\rm AF}$ is expressed as [33, 34]

$$J_{\rm AF} \approx -\frac{(\Delta\varepsilon)^2}{U_{\rm eff}} \tag{1}$$

where $U_{\rm eff}$ is the effective on-site repulsion, which is essentially constant for a given compound. If the two spin sites are equivalent, $\Delta\varepsilon$ is the energy difference $\Delta E$ between the two magnetic orbitals representing the spin dimer. When the two spin sites are nonequivalent, $(\Delta\varepsilon)^2 = (\Delta E)^2 - (\Delta E^0)^2$, where $\Delta E^0$ is the energy difference between the magnetic orbitals representing each spin site of the spin dimer ($\Delta E^0 = 0$ if the two spin sites are equivalent).

In our case, the $\Delta E$ and $\Delta E^0$ values for various spin dimers are evaluated by performing extended Hückel tight binding (EHTB) calculations[35]. For a variety of magnetic solids of transition-metal ions, it has been found that their magnetic properties are well described by the $(\Delta\varepsilon)^2$ values obtained from EHTB calculations [36], when both the *d* orbitals of the transition metal and s/p orbitals of its surrounding ligands are represented by double-ζ–Slater-type orbitals (DZ–STO) [37]. Our calculations were carried out using the atomic parameters summarized in table 1. A radial part of the DZ–STO is expressed as

$$r^{n-1}\left[c_1 \exp\left(-\zeta_1 r\right) + c_2 \exp\left(-\zeta_2 r\right)\right], \tag{2}$$

where $n$ is the principal quantum number and the exponents $\zeta_1$ and $\zeta_2$ describe contracted and diffuse STOs, respectively (i.e., $\zeta_1 > \zeta_2$). The $(\Delta\varepsilon)^2$ values are a sensitive function of the exponent $\zeta_2$ of the diffuse O 2p orbital. The $\zeta_2$ values taken from the results of electronic structure calculations for neutral atoms may not be contracted enough to describe $O^{2-}$ ions [37]. To make the O 2p orbital more contracted, the $\zeta_2$ value should be increased. To quantify how the contraction of the O 2p orbital affects the relative strengths of the spin exchange interactions, we replace $\zeta_2$ with $(1 + x)\zeta_2$ and calculate the $(\Delta\varepsilon)^2$ values for $x = 0.00,\ 0.025,$ and 0.05.

The relative values of $(\Delta\varepsilon)^2$ for the superexchange (SE) paths $J_1$, $J_2$, and $J_3$ are summarized in table 2. The strongest SE interaction takes place through $J_2$, while the weakest SE interaction occurs through $J_3$. $J_1$ lies between $J_2$ and $J_3$ for all $x$. These results are compatible with the fact that the bond angle Cu1–O1–Cu3 of $J_2$ is slightly larger than that Cu1–O1–Cu2 of $J_1$, i.e. 119.2° versus 111.4°, respectively. In addition, $J_3$ is mediated by two exchange paths Cu2–O1–Cu3 and Cu2–O2–Cu3 but their bond angles of 95.8 and 101.1° are smaller than

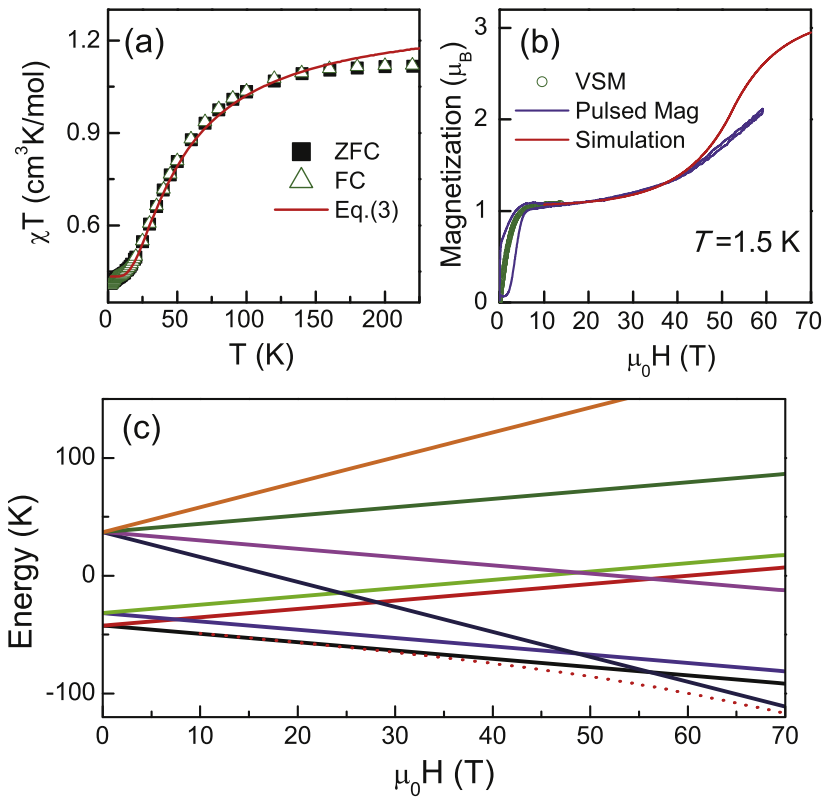


**Figure 2.** (a) $\chi(T)T$ versus $T$ of ($Cu_3(OH)$) for field cooling (green open triangles) and zero-field cooling (black full squares) measured in an external field of $\mu_0 H = 0.1$ T. The solid line is a fit to equation (3). (b) Magnetization curve measured at $T = 1.5$ K by using VSM (green open circles) in a field range of $\mu_0$H = 0–14 T as well as by using a pulsed field magnetometer (blue solid lines) in a field range of $\mu_0$H = 0–60 T together with the numerically simulated magnetization curve (red solid line) based on the dynamic magnetization process equation (4). (c) Energy level diagram determined by the spin Hamiltonian (3). See the text for fitting parameters.

those of $J_1$ and $J_2$. The relative strengths of the spin exchange interactions obtained from the spin dimer analysis give a reasonable description of magnetic behaviors, which will be discussed in the following section.

### 3.2. Magnetic susceptibility and magnetization

Figure 2(a) shows $\chi(T)T$ versus $T$ measured in the temperature range of T = 2–220 K at an external field of $\mu_0 H = 0.1$ T. $\chi(T)T$ is weakly temperature dependent in the temperature range of 120–220 K and then decreases rapidly for temperatures below 120 K. The nearly constant $\chi(T)T$ at higher temperatures is associated with the mixture of both $S^T = 1/2$ and $S^T = 3/2$ spin states while the decrease of $\chi(T)T$ at lower temperatures is due to the predominant occupation of the $S^T = 1/2$ state over the $S^T = 3/2$ one. We find no difference between field-cooling and zero-field-cooling data. This is consistent with a $S^T = 1/2$ ground state.

Since $S = 1/2$ $Cu^{2+}$ ions in the scalene triangle ($Cu_3(OH)$) are coupled by Heisenberg exchange interactions, the minimal spin Hamiltonian in an external field can be written as

$$\hat{H} = J_1 \mathbf{S}_1 \cdot \mathbf{S}_2 + J_2 \mathbf{S}_2 \cdot \mathbf{S}_3 + J_3 \mathbf{S}_3 \cdot \mathbf{S}_1 - g\mu_B \mathbf{H} \cdot \sum_{i=1}^{3} \mathbf{S}_i, \quad (3)$$

where $g$ is the average $g$-factor, $\mu_B$ is the Bohr magneton, $J_i$ is the exchange coupling constant, and $\mathbf{S}_i$ is the spin operator. For a realistic Hamiltonian, Dzyaloshinskii–Moriya (DM) interactions and a site-dependent $g$-tensor should be added to equation (3) as ($Cu_3(OH)$) has the structural distortions from an equilateral triangle. We note that the Hamiltonian (3) cannot open anti-crossing energy gaps between the $S^T = 1/2$ and the $S^T = 3/2$ state. As a consequence, the magnetization jumps in a magnetization curve cannot be described strictly within this Hamiltonian (see figure 2(b)). Since the level crossings occur around 50 T, however, it is practically impossible to determine uniquely all possible magnetic parameters including DM interactions. Therefore, we will proceed with the Hamiltonian (3) for the sake of simplicity.

For the calculation of the equilibrium magnetization, we used the MAGPACK software, which employs an irreducible tensor operator technique [39]. We obtain a satisfactory agreement between the theoretical and the magnetic susceptibility data with the fitting parameters $J_1 = -43.5$ K, $J_2 = -53.0$ K, and $J_3 = -37.7$ K, and

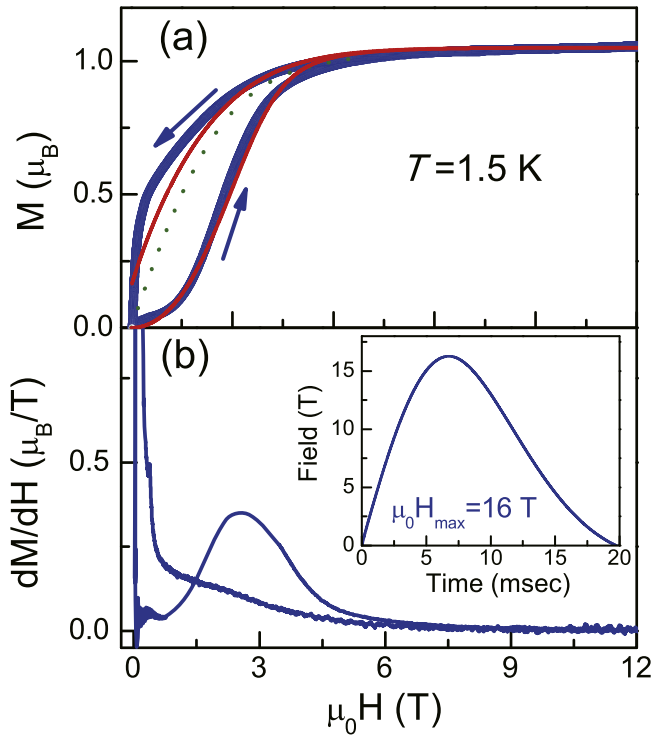


**Figure 3.** (a) Hysteresis loop (open circles) measured at $T = 1.5$ K using a fast sweeping pulsed field with a maximum field of $\mu_0 H_{\max} = 16$ T. The dotted line is the equilibrium magnetization measured by VSM. The red line is the simulated magnetization curve. (b) Derivative d$M$/d$H$ of the magnetization curve. The sharp peak at zero field in d$M$/d$H$ corresponds to magnetization jump. The inset plots the time dependence of a pulsed magnetic field.

$g = 2.16$ (see the solid line in figure 2(a)). We note that the determined $g$-factor corresponds to an average of $Cu^{2+}$ ions (see section 3.3). In addition, the magnetic parameters are in line with the ratios of $J_i$ extracted from the spin dimer analysis as listed in table 2.

Based on the obtained fitting parameters, we determine the energy level diagram versus an applied magnetic field as plotted in figure 2(c). The two degenerated $S^T = 1/2$ states are lifted due to strong distortions to an scalene triangle. The splitting energy between doublets amounts to about 10 K, which corresponds to an average of the energy difference between $J_i$, that is, $|J_i - J_j| = 5.8$–$15.3$ K. The energy separation between the $S^T = 1/2$ doublet and $S^T = 3/2$ quartet state is given by about 70 K. The $S^T = 1/2$ state crosses successively with the $S^T = 3/2$ state at $\mu_0 H_{c1} = 48$ and $\mu_0 H_{c2} = 56$ T. This induces a field-induced switching of the ground state to the $S^T = 3/2$ state, leading to the $2\mu_B$ magnetization jump. In figure 2(b) we plot the pulsed field magnetization curve (violet lines) along with the static field magnetization one (green open circles).

To crosscheck the validity of the determined magnetic parameters, we simulate the pulsed field magnetization curve as detailed below. In doing that, we introduce the anti-crossing energy gap at $\mu_0 H_c = 56$ T (see equation (7)), which is absent in equation (3). The resulting ground state is shown as the dashed line in figure 2(c). This procedure is justified because the distorted triangle cluster usually hosts the DM interaction, allowing an avoided level crossing gap [15, 23, 24]. In contrast to the magnetization below 15 T, the pulsed field magnetization above 15 T lacks hysteresis. Thus, the equilibrium magnetization process may suffice to describe the high-field magnetic behavior. The equilibrium magnetization is calculated with a usual thermodynamic average. Due to a large energy separation between the ground and the first excited states only the ground state is relevant. The nice agreement between the calculated and the experimental curve is found for fields up to 40 T (see the red line in figure 2(b)). The discrepancy seen for fields above 40 T may be due to the presence of another avoided level crossing at 48 T in the upper doublet state, which is not considered in the equilibrium magnetization simulation. The magnetization process below 15 T will be discussed below.

We measured hysteresis loop with the maximum pulse field of $\mu_0 H_{\max} = 16$ T. As shown in figure 3(a), the detailed feature of $M(H)$ relies on the time structure of a pulse field (see the inset of figure 3(b)). In the up sweep, the pulsed field magnetization is smaller than the equilibrium one while in the down sweep it becomes bigger. This means that a spin temperature is significantly higher (lower) than a bath temperature in the up (down) sweep. We take the derivative of the magnetization, d$M$ ($H$)/d$H$ to detail the magnetization structure. The results are plotted in figure 3(b). We can identify a sharp peak at a zero field, suggesting the presence of a zero-

field gap. When a field sweep is sufficiently slow, the transition probability between the $S^T = 1/2$ levels is determined by the Landau–Zener–Stückelberg (LZS) model and their populations equilibrate with the Boltzmann distribution through spin–phonon transitions. In a fast field sweep, a majority of spins in the higher $S^T = 1/2$ levels are out of equilibrium because the energy flow from the lattice to the spins is not sufficient to reach equilibrium. Indeed, the field sweep rate of $4 - 8 \times 10^{-4}$ T s$^{-1}$ is comparable to the electron spin–lattice relaxation time of $T_1 \sim 10^{-4}$s (*vide infra*). As a consequence, the spin temperature is higher than the cryostat temperature. In the down sweep, conversely, the field variation is too fast for the spins in the lower $S^T = 1/2$ levels to populate to the higher levels.

To describe this behavior quantitatively, we simulate numerically the magnetization hysteresis based on the Bloch-type master equation [40, 41]

$$\frac{\mathrm{d}}{\mathrm{d}t}M_d(t,\,\theta) = \frac{1}{\tau(T,\,B(t),\,\theta)}\Big[M_{\mathrm{eq}}(T,\,B(t),\,\theta) - M_d(t,\,\theta)\Big], \tag{4}$$

where $\tau$ is the relaxation time and $M_{\mathrm{eq}}(M_d)$ is the equilibrium (dynamic) magnetization as a function of time and angle $\theta$. The relaxation rate comprises three terms $1/\tau = 1/\tau_{\mathrm{thermal}} + 1/\tau_{\mathrm{LZS}} + 1/\tau_{\mathrm{res}}$: (i) thermal relaxation $1/\tau_{\mathrm{thermal}}$, (ii) LZS transition $1/\tau_{\mathrm{LZS}}$, and (iii) residual relaxation $1/\tau_{\mathrm{res}}$. $1/\tau_{\mathrm{res}}$ represents the relaxation processes other than the thermal relaxation.

Among different thermal relaxation processes, we consider a single-phonon relaxation process given as [42]

$$\begin{aligned} 1/\tau_{\mathrm{thermal}} &= \frac{3g^3\mu_B^3V_{\mathrm{sp}}^2}{2\pi\rho v^5\hbar^4}B(t)^3\,\coth\left[\frac{g\mu_B B(t)}{2k_BT}\right] \\ &= AB(t)^3\,\coth\left[\frac{g\mu_B B(t)}{2k_BT}\right], \end{aligned} \tag{5}$$

where $g$ is the Lande $g$-factor, $\rho$ is the mass density, $v$ is the sound velocity, $B(t)$ is the time-varying field strength and $V_{\mathrm{sp}}$ is the characteristic energy modulation of the spin–phonon coupling mechanism.

The LZS transition rate is related to the LZS transition probability $P_{\mathrm{LZS}}$ through $1/\tau_{\mathrm{LZS}} = \alpha P_{\mathrm{LZS}}$ where $\alpha$ is a proportionality constant. $P_{\mathrm{LZS}}$ is given as [43]

$$P_{\mathrm{LZS},M\to M'} = 1 - \exp\left(-\frac{\pi\Delta_{M,M'}^2}{2\hbar g\mu_B\,|M-M'|\,\frac{\mathrm{d}B}{\mathrm{d}t}}\right). \tag{6}$$

Here $\Delta_{M,M'}^2$ is the anti-crossing energy gap between the two states with spin quantum number $M$ and $M'$ expressed as [41]

$$\Delta_{M,M'}^2 = \sqrt{\left(\Delta_{\mathrm{zf}}\right)^2 + \left[g\mu_B(M-M')B\right]^2} - \left|g\mu_B(M-M')B\right|, \tag{7}$$

where $\Delta_{\mathrm{zf}}$ is the minimum energy gap between unperturbed energy levels.

Best fits of the experimental data were obtained with the parameters: $A = 81.0$ Hz T$^{-3}$, $1/\tau_{\mathrm{res}} = 324.0$ Hz, $\Delta_{\mathrm{zf}} = 5.1$ K and $\alpha = 1386$ Hz. The simulated curve is plotted as the red solid lines in figure 3(a). As can be seen, the simulation reproduces reasonably the up sweep of the hysteresis loop. However, there is a noticeable discrepancy between the calculated and experimental magnetization curve in the down sweep. This may be due to the fact that the thermal relaxation rate is not described within the single-phonon relaxation process (see section 3.4). Further, it should be noted that the anti-crossing gap $\Delta_{\mathrm{zf}}$ at $\mu_0 H = 0$ T is much larger than the magnitude of intermolecular dipole and hyperfine interactions. This indicates that the zero-field magnetization jump is linked to the energy splitting between the doublets rather than in the intra-doublets.

### 3.3. CW electron paramagnetic resonance

Figure 4(a) shows the temperature dependence of the EPR signal recorded at $\nu = 240$ GHz. At $T = 5$ K, a single peak originates from the electron spin transition between the $S^T = 1/2$ level, i.e., $|\frac{1}{2};\,-\frac{1}{2}\rangle \to |\frac{1}{2};\,\frac{1}{2}\rangle$. With increasing temperature, the signal shifts to lower fields and broadens. We plot the temperature dependences of the peak-to-peak linewidth ($\Delta H_{\mathrm{pp}}$) and resonance field ($H_{\mathrm{res}}$) in figures 4(b) and (c). $\Delta H_{\mathrm{pp}}(T)$ [$H_{\mathrm{res}}(T)$] increases (decreases) in a monotonic manner for temperatures above 30 K. This is attributed to a gradual population of spins to the excited $S^T = 3/2$ levels. At high temperatures, the EPR signal is given by a sum of the three resonance lines; $|\frac{3}{2};\,-\frac{3}{2}\rangle \to |\frac{3}{2};\,-\frac{1}{2}\rangle$, $|\frac{3}{2};\,-\frac{1}{2}\rangle \to |\frac{3}{2};\,\frac{1}{2}\rangle$, and $|\frac{3}{2};\,\frac{1}{2}\rangle \to |\frac{3}{2};\,\frac{3}{2}\rangle$. Due to the structural distortions and anisotropies, the energy separation between the higher levels increases slightly. This leads to the shift of $H_{\mathrm{res}}(T)$ to lower fields and the increase of $\Delta H_{\mathrm{pp}}$ at elevated temperatures.

Figure 5 shows the angular dependence of the EPR spectra recorded at $T = 5$ K by varying from −2° to 179°. The angle is measured between the triangle plane and the external magnetic field. The angular dependence of

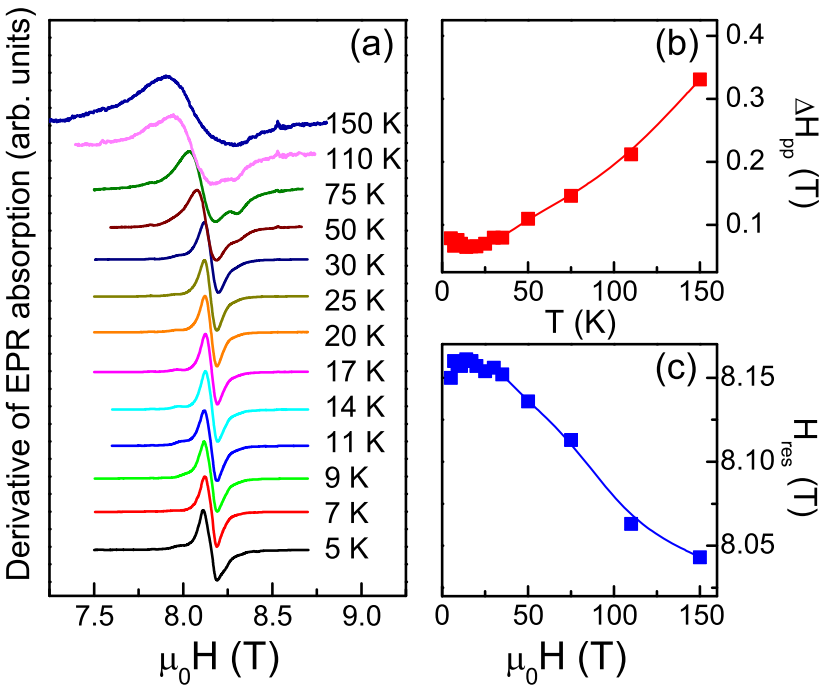


**Figure 4.** (a) Derivative of the EPR absorption of ($Cu_3$(OH)) measured at $\nu = 240$ GHz as a function of temperature. (b) and (c) temperature dependences of the the peak-to-peak linewidth, $\Delta H_{pp}(T)$, and the resonance field, $H_{res}(T)$, respectively. The solid lines are guides to the eyes.

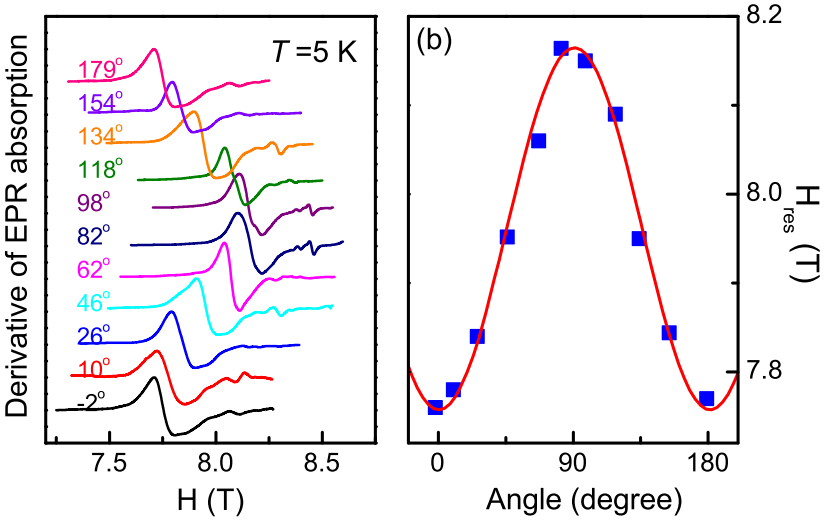


**Figure 5.** (a) Angular dependence of the EPR spectra (derivative of the absorption spectra versus field, vertically shifted for clarity) measured at $\nu = 240$ GHz and at $T = 5$ K. (b) Angular dependence of the resonance fields. The solid line is a fit to the conventional expression $H_{res} = \sqrt{H_\perp \sin^2\theta + H_\parallel \cos^2\theta}$.

$H_{res}(T)$ is described by the standard relation $H_{res} = \sqrt{H_\perp \sin^2\theta + H_\parallel \cos^2\theta}$, where $H_\perp$ and $H_\parallel$ is the resonance field perpendicular and parallel to the triangular plane, respectively. By using the relation $g = h\nu/\mu_B H_{res}$, we can determine anisotropy in $g$-factors, $g_\perp = 2.10(4)$ and $g_\parallel = 2.21(3)$. The substantial deviation of the $g$-factor from 2 confirms the structural analysis that shows the axial elongation of square pyramid environments.

### 3.4. Pulsed EPR

To characterize spin decoherence processes, we performed a 240 GHz pulsed EPR experiment. The spin–lattice relaxation time $T_1$ was measured by using an inversion-recovery pulse sequence ($\pi - t - \pi/2 - \tau - \pi - \tau -$ echo) with varying $t$ and fixed $\tau = 300$ ns. The maximum available power is about 20 mW and the typical $\pi/2$ pulse length is 260 ns. Figure 6(a) shows the echo decay curve recorded at $\mu_0 H = 7.813$ T and $T = 1.45$ K. It is fitted to a double

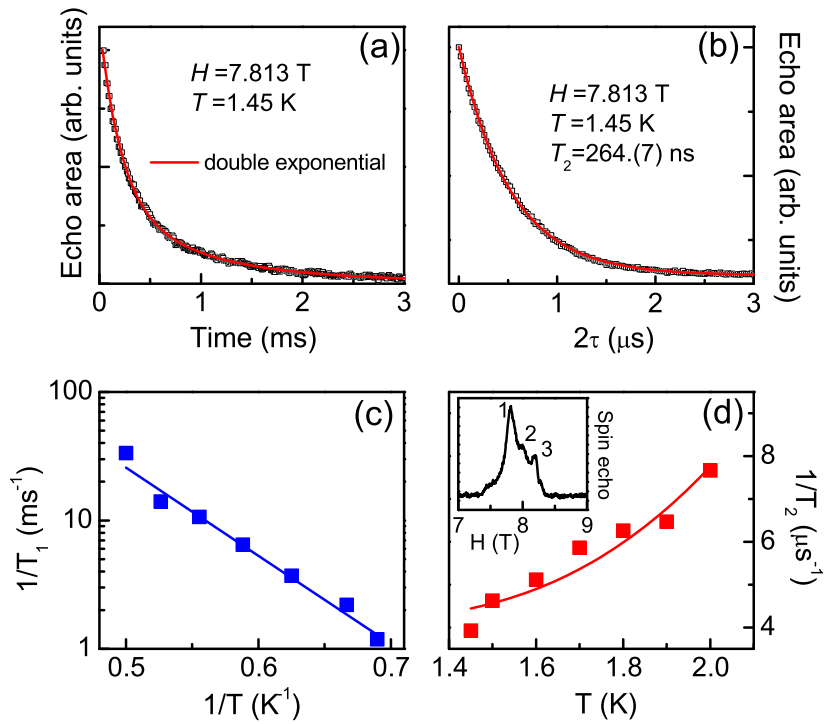


**Figure 6.** (a) Echo decay measured by a recovery pulse sequence at $\mu_0 H = 7.813$ T and $T = 1.45$ K. The red solid line is a fit to a double exponential function. (b) Decay of the integrated Hahn echo area as a function of delay time, $2\tau$. The red solid line is a fit to a single exponential function. (c) A spin–lattice relaxation rate, $1/T_1$, versus $1/T$ in a semi-logarithmic scale. The solid line is a fit to an activation function, $1/T_1 \propto \exp(-\Delta/T)$. (d) Temperature dependence of a spin–spin relaxation rate, $1/T_2$. The solid line is a fit to equation (8). The inset shows a spin-echo signal recorded by sweeping an external field at $T = 1.5$ K.

exponential function, $I = A \exp(-T/T_{\text{long}}) + B \exp(-T/T_{\text{short}})$ with $T_{\text{long}} = 153$ $\mu$s and $T_{\text{short}} = 63$ $\mu$s. The short $T_1$ is likely related to a fast spectral diffusion while the long $T_1$ pertains to the spin–lattice relaxation time. The spectral diffusion can be caused by molecular motion, exchange interactions, nuclear spin flip-flops, or electron–nuclear cross-relaxation. Here we note that the obtained $T_1$ is shorter than that of ($Cu_3$–$X$) by a factor two [31].

Figure 6(c) plots $1/T_1$ versus $1/T$ in a semi-logarithmic scale. The spin echo signal becomes significantly weak for temperatures above 2.4 K so that $T_1$ cannot be unambiguously measured for $T > 2.4$ K. In general, a spin–lattice relaxation rate is given by a combination of three terms [42]: (i) direct process with $1/T_1 \propto \coth(\hbar\omega/2k_BT)$, (ii) Raman process with $1/T_1 \propto T^{3+2m}$ where $m$ is the spectral dimensionality, and (iii) Orbach process with $1/T_1 \propto 1/[\exp(\Delta_O/k_BT) - 1]$. We find that our data are well described by an activation form $1/T_1 \propto \exp(-\Delta_O/T)$ with $\Delta_O = 7.4(6)$ K. This corresponds to the approximation of the Orbach process when $\Delta_O \gg k_BT$. This suggests that the Orbach process governs the relaxation in a low-temperature regime. We note that the Raman process is negligible as the $T_1$ calculation for the ($V_{15}$) cluster shows [44]. In addition, the direct process is temperature independent at low temperatures. The Orbach process involves a transfer of spins between the ground doublet $S^T = 1/2$ via phonons. Thus, the relaxation rate relies on the number of phonons with energy $\Delta_O$. Noticeably, the intra-doublet splitting of $\Delta = 10.2(3)$ K at $\mu_0 H = 7.813$ T is close to the value of $\Delta_O = 7.4(6)$ K. Therefore, we conclude that the Orbach process takes place through the transition between the $S^T = 1/2$ states. This is further supported by the failure of the single-phonon relaxation process in describing the dynamic magnetization process discussed above. We note that our result is contrasted with the case of ($Cu_3$–$X$) where the spin–lattice relaxation is dominated by a direct process [31]. The absence of the Orbach process in ($Cu_3$–$X$) can be ascribed to a small energy scale of $J_i$, which is one order of magnitude smaller than that of ($Cu_3$(OH)).

Using the standard Hahn echo pulse sequence ($\pi/2 - \tau - \pi - \tau -$ echo) we measured the variation of a spin–spin relaxation time, $T_2$ with temperature. Figure 6(b) exhibits decay of the integrated Hahn echo at $\mu_0 H = 7.813$ T (the transition 1 in the inset of figure 6(d)) as a function of the delay time $2\tau$. The echo intensity decay is fitted to a single exponential function $I \propto \exp(-2\tau/T_2)$ with $T_2 = 264.(7)$ ns at $T = 1.45$ K.

From extensive theoretical and experimental works [14, 15, 45], it is well known that for molecular magnets, decoherence is solely determined by three environmental sources: (i) phonons, (ii) nuclear spins, and (iii) intermolecular dipolar interactions. The environmental decoherence time for ($Fe_8$) can be theoretically extended up to about 500 $\mu$s by optimizing temperature and external fields. Under accessible experimental

conditions, however, the decoherence time is limited to an order of microseconds: $T_2 \sim 0.63\ \mu$s for ($Fe_8$) [14], 0.34 $\mu$s for ($V_{15}$) [15], and 0.75 $\mu$s for ($Cu_3$–$X$) molecule magnet [31]. The nuclear spins were identified as a main source of decoherence for ($V_{15}$), in which $T_2$ was measured at a low field of $\mu_0 H = 0.336$ T [15]. Takahashi *et al* [14] have shown that at high fields the nuclear spin decoherence becomes less significant than the dipolar and the phonon decoherence. As $T_2$ of ($Cu_3$(OH)) was determined at a high field of $\mu_0 H = 7.813$ T, we expect an appreciable contribution of a $T_1$ mechanism to decoherence in case of ($Cu_3$(OH)) in contrast to ($V_{15}$).

Similar to the $T_1$ relaxation time, $T_2 \sim 0.26\ \mu$s of ($Cu_3$(OH)) is also reduced by several factors compared to that of ($Cu_3$–$X$). Since both ($Cu_3$(OH)) and ($Cu_3$–$X$) were measured at the same field and contain the same type of nuclear spins, the shortening of $T_2$ in ($Cu_3$(OH)) is mainly caused by the Orbach mechanism.

Lastly, we turn to the temperature dependence of $1/T_2$. Under a high external field of $\mu_0 H = 7.813$ T, most of the spins are polarized to the $|\frac{1}{2}; -\frac{1}{2}\rangle$ state and thus a spin flip-flop process is mainly responsible for the $T$-dependence of $1/T_2$ [46]. This is modeled by a spin bath fluctuation theory [45, 47];

$$\frac{1}{T_2} = A \sum_{m_S=1}^{7} W(m_S) P(m_S) P\left(m_S + 1\right) + \Gamma_{\rm res}, \tag{8}$$

where A is a temperature independent parameter, $\Gamma_{\rm res}$ a residual relaxation rate, $W(m_S)$ the flip-flop transition probability for the $m_S$th state with $\Delta m_S = \pm 1$, and $P(m_S) = \exp(-E(m_S)/k_B T)/Z$, where $Z$ is the partition function. The experimental data agree with the theoretical calculation obtained by equation (8) with the fitting parameters $W(1) = 1.2(2)\mu s^{-1}$ and $\Gamma_{\rm res} = 4.0(7)\mu s^{-1}$. This result does not necessarily contradict the above conclusion that the phonon process is substantially involved in decoherence. This is because the measured temperature window of T = 1.45–2.4 K is rather narrow to examine an additional contribution from the Orbach process which has the similar functional form and energy gap of $\Delta_O = 7.4(6)$ K as the spin bath theory.

## 4. Conclusions

We have presented detailed magnetization, EPR, and relaxation measurements as well as microscopic magnetic calculations on the newly synthesized magnetic cluster ($Cu_3$(OH)). This molecule magnet realizes a strongly distorted scalene triangle with the antiferromagnetic coupling constants $J_1 = -43.5$ K, $J_2 = -53.0$ K, and $J_3 = -37.7$ K. By using a 240 GHz pulsed EPR we evaluated the relaxation times $T_1$ and $T_2$. $T_1$ is an order of $10^{-4}$ s at $T = 1.5$ K. The temperature dependence of $1/T_1$ is governed by Orbach process at low temperatures. A spin decoherence time is determined to be $T_2 \sim 0.26\ \mu$s. The temperature dependence of $1/T_2$ is well described by spin bath fluctuations. Compared to the isosceles triangle ($Cu_3$–$X$), the $T_1$ and $T_2$ times are reduced by several factors. Since the Orbach process is present only in ($Cu_3$(OH)), the shortening of a spin decoherence time is caused by the additional spin–phonon mechanism in spin triangular clusters.

## Acknowledgments

The National High Magnetic Field Laboratory is supported by NSF Cooperative Agreement No. DMR-1157490, and by the State of Florida. KYC and HJK acknowledge financial support from Korea NRF Grant (No. 2009-0093817, 2010-0021042, and No. 2012-046138). We acknowledge the support of the HLD at HZDR, member of the European Magnetic Field Laboratory (EMFL).

## References

[1] Gatteschi D, Sessoli R and Villain J 2006 *Molecular Nanomagnets* (New York: Oxford University Press)
[2] Bogani L and Wernsdorfer W 2008 *Nat. Mater.* **7** 179
[3] Leuenberger M N and Loss D 2001 *Nature* **410** 789
[4] Clemente-Juan J M, Coronado E and Gaita-Arino A 2012 *Chem. Soc. Rev.* **41** 7464
[5] Thomas L, Lionti F, Ballou R, Gatteschi D, Sessoli R and Barbara B 1996 *Nature* **383** 145
Stamp P C E 1996 *Nature* **383** 125 (see for news and views)
[6] Julien M-H, Jang Z H, Lascialfari A, Borsa F, Horvatic M, Caneschi A and Gatteschi D 1999 *Phys. Rev. Lett.* **83** 227
[7] Furrer A and Waldmann O 2013 *Rev. Mod. Phys.* **85** 367 (see for reviews)
[8] Chiolero A and Loss D 1998 *Phys. Rev. Lett.* **80** 169
[9] Barbara B and Chudnoversusky E M 1990 *Phys. Lett.* A **145** 205
Platonov V V, Tatsenko O M, Plis V I, Popov A I, Zvezdin A K and Barbara B 2002 *Phys. Solid State* **44** 2104
[10] Waldmann O, Dobe C, Mutka H, Furrer A and Gudel H U 2005 *Phys. Rev. Lett.* **95** 057202
[11] Wernsdorfer W and Sessoli R 1999 *Science* **284** 133
[12] Miyashita S 1996 *J. Phys. Soc. Japan* **65** 2734
de Raedt H, Miyashita S, Saito K, Garcia-Pablos D and Garcia N 1997 *Phys. Rev.* B **56** 11761
Miyashita S, Saito S and de Raedt H 1998 *Phys. Rev. Lett.* **80** 1525

Dobrovitski V V and Zverdin A K 1997 *Europhys. Lett.* **38** 377
Gunther L 1997 *Europhys. Lett.* **39** 1
[13] Hill S, Edwards R S, Aliaga-Alcalde N and Christou G 2003 *Science* **302** 1015
[14] Takahashi S, Tupitsyn I S, Tol J, van, Beedle C C, Hendrickson D N and Stamp P C E 2011 *Nature* **476** 76
[15] Bertaina S, Gambarelli S, Mitra T, Tsukerblat B, Müller A and Barbara B 2008 *Nature* **453** 203
[16] Tsukerblat B and Tarantul A 2010 *Molecular Cluster Magnets* ed R E P Winpenny (Singapore: World Scientific) (see for reviews on ($V_{15}$) cluster)
[17] Muller A and Doring J 1988 *Angew. Chem. Int. Ed.* **27** 1719
[18] Chiorescu I, Wernsdorfer W, Müller A, Bögge H and Barbara B 2000 *Phys. Rev. Lett.* **84** 3454
[19] Chaboussant G, Basler R, Sieber A, Ochsenbein S T, Desmedt A, Lechner R E, Telling M T F, Kögerler P, Müller A and Güdel H-U 2002 *Europhys. Lett.* **59** 291
[20] Rousochatzakis I, Ajiro Y, Mitamura H, Kögerler P and Luban M 2005 *Phys. Rev. Lett.* **94** 147204
[21] Luban M *et al* 2002 *Phys. Rev.* B **66** 054407
[22] Trif M, Troiani F, Stepanenko D and Loss D 2008 *Phys. Rev. Lett.* **101** 217201
[23] Choi K-Y, Matsuda Y H, Nojiri H, Kortz U, Hussain F, Stowe A C, Ramsey C and Dalal N S 2006 *Phys. Rev. Lett.* **96** 107202
[24] Choi K-Y, Dalal N S, Reyes A P, Kuhns P L, Matsuda Y H, Nojiri H, Mal Sib S and Kortz U 2008 *Phys. Rev.* B **77** 024406
[25] Luzon J, Bernot K, Hewitt I J, Anson C E, Powell A K and Sessoli R 2008 *Phys. Rev. Lett.* **100** 247205
[26] Nath R *et al* 2013 *Phys. Rev.* B **87** 214417
[27] Müller A, Luban M, Schröder C, Modler R, Kögerler P, Axenovich M, Schnack J, Canfield P C, Budko S and Harison N 2001 *Chem. Phys. Chem.* **2** 517
[28] Carretta S, Santini P, Amoretti G, Troiani F and Affronte M 2007 *Phys. Rev.* B **76** 024408
[29] Troiani F and Affronte M 2001 *Chem. Soc. Rev.* **40** 3119
[30] Aromi G, Aguila D, Gamez P, Luis F and Roubeau O 2012 *Chem. Soc. Rev.* **41** 537
[31] Choi K-Y, Wang Z, Nojiri H, Tol J van, Kumar P, Lemmens P, Bassil B S, Kortz U and Dalal N S 2012 *Phys. Rev. Lett.* **108** 067206
[32] Skourski Y, Kuz'min M D, Skokov K P, Andreev A V and Wosnitza J 2011 *Phys. Rev.* B **83** 214420
[33] Whangbo M-H, Koo H-J and Dai D J 2003 *Solid State Chem.* **176** 417 (see for reviews)
Whangbo M-H, Dai D J and Koo H-J 2005 *Solid State Sci.* **7** 827
[34] Hay P J, Thibeault J C and Hoffmann R 1975 *J. Am. Chem. Soc.* **97** 4884
[35] Hoffmann R 1963 *J. Chem. Phys.* **39** 1397
[36] Koo H-J and Whangbo M-H 2001 *Inorg. Chem.* **40** 2169
[37] Clementi E and Roetti C 1974 *At. Data Nucl. Data Tables* **14** 177
[38] Ammeter J, Bürgi H-B, Thibeault J and Hoffmann R 1974 *J. Am. Chem. Soc.* **100** 3686
[39] Borrás-Almenar J J, Clemente-Juan J M, Coronado E and Tsukerblat B S 2001 *J. Comput. Chem.* **22** 985
[40] Rousochatzakis I, Ajiro Y, Mitamura H, Kögerler P and Luban M 2005 *Phys. Rev. Lett.* **94** 147204
Rousochatzakis I and Luban M 2005 *Phys. Rev.* B **72** 134424
[41] Park J-N, Suh B J, Choi K Y, Nojiri H and Jang Z H 2007 *J. Korean Phys. Soc.* **50** 464
[42] Abragam A and Bleaney B 1970 *Electron Paramagnetic Resonance of Transition Ions* (Oxford: Clarendon)
[43] Wernsdorfer W, Bhaduri S, Vinslava A and Christou G 2005 *Phys. Rev.* B **72** 214429
[44] Tarantul A and Tsukerblat B 2011 *J. Phys.: Conf. Ser.* **324** 012007
[45] Stamp P C E and Tupitsyn I S 2004 *Phys. Rev.* B **69** 014401
Morello A, Stamp P C E and Tupitsyn I S 2006 *Phys. Rev. Lett.* **97** 207206
Prokof'ev N V and Stamp P C E 2000 *Rep. Prog. Phys.* **63** 669
[46] Takahashi S, Hanson R, Van T J, Sherwin M S and Awschalom D D 2008 *Phys. Rev. Lett.* **101** 047601
[47] Kutter C, Moll H P, Van T J, Maan J C and Wyder P 1995 *Phys. Rev. Lett.* **74** 2925